INORGANIC CHEMISTRY FRONTIERS

RESEARCH ARTICLE

View Article Online
View Journal | View Issue

Cite this: *Inorg. Chem. Front.*, 2024, **11**, 8660

Optimizing the spin qubit performance of lanthanide-based metal–organic frameworks†

Xiya Du [a,b,c] and Lei Sun *[b,c,d]

Received 12th September 2024,
Accepted 26th October 2024

DOI: 10.1039/d4qi02324b

rsc.li/frontiers-inorganic

Lanthanide-based spin qubits are intriguing candidates for high-fidelity quantum memories owing to their spin-optical interfaces. Metal–organic frameworks (MOFs) offer promising solid-state platforms to host lanthanide ions because their bottom-up synthesis enables rational optimization of both spin coherence and luminescence. Here, we incorporated Nd^{3+} and Gd^{3+} into a La^{3+}-based MOF with various doping levels and examined their qubit performance including the spin relaxation time (T_1) and phase memory time (T_m). Both Nd^{3+} and Gd^{3+} behave as spin qubits with T_1 exceeding 1 ms and T_m approaching 2 μs at 3.2 K at low doping levels. Variable-temperature spin dynamic studies unveiled spin relaxation and decoherence mechanisms, highlighting the critical roles of spin–phonon coupling and spin–spin dipolar coupling. Accordingly, reducing the spin concentration, spin–orbit coupling strength, and ground spin state improves the qubit performance of lanthanide-based MOFs. These optimization strategies serve as guidelines for the future development of solid-state lanthanide qubits targeting quantum information technologies.

Introduction

Quantum memories are indispensable building units for distributed quantum computing and optical-fiber-based quantum communication.[1–3] They can interconvert the quantum state between a flying qubit, typically a photon, and a stationary qubit that is insensitive to the environment, allowing on-demand storage and extraction of quantum information.[4,5] Paramagnetic lanthanide (rare earth) ions, *e.g.* Ce^{3+}, Nd^{3+}, Eu^{3+}, Er^{3+}, Pr^{3+} and Yb^{3+}, are promising candidates for stationary qubits thanks to their spin coherence and narrow and well-defined emission lines.[6–11] When embedded in inorganic crystals such as Y_2O_3 and Y_2SiO_5, they could maintain quantum coherence over 1 ms at approximately 10 mK.[12,13] Meanwhile, the mapping between their emission wavelengths and spin sublevels promotes coherent addressing of single qubits by optically detected magnetic resonance.[5,14] These advantages have inspired the development of lanthanide-based quantum memories that can store photons for over one hour.[15]

Spin–photon transduction requires lanthanide qubits with a long spin decoherence time (T_2) and high optical addressing fidelity.[16] While the latter can be improved by integrating lanthanide qubits into nanophotonic cavities,[17,18] the optimization of T_2 demands sophisticated material design. T_2 is upper bound by twice the spin relaxation time (T_1), which often decreases sharply with an increase in temperature for lanthanide qubits stemming from their strong spin–phonon coupling.[19,20] The strength of spin–phonon coupling may be weakened by tweaking the phonon dispersion relations of solid-state matrices.[21] Nonetheless, this requires fine tuning of the crystal structures of host materials, especially coordination environments of lanthanide ions, which is unfeasible for inorganic solids.[22]

Metal–organic frameworks (MOFs) offer tunable solid-state matrices for lanthanide qubits. MOFs are crystalline and microporous materials consisting of metal ions and organic ligands.[23] Their spatial ordering and bottom-up assembly of constituents facilitate the rational design of crystal structures and in turn phonon dispersion relations.[24,25] Meanwhile, lanthanide ions could be incorporated into MOFs with controlled spatial distribution and coordination environments.[26,27] These advantages would allow the strategic suppression of spin relaxation and decoherence.[28,29] Indeed, recent studies on molecular lanthanide qubits have revealed

[a]*Department of Chemistry, Zhejiang University, Hangzhou, Zhejiang Province 310058, China*
[b]*Department of Chemistry, School of Science and Research Center for Industries of the Future, Westlake University, Hangzhou, Zhejiang Province 310030, China. E-mail: sunlei@westlake.edu.cn*
[c]*Institute of Natural Sciences, Westlake Institute for Advanced Study, Hangzhou, Zhejiang Province 310024, China*
[d]*Key Laboratory for Quantum Materials, Department of Physics, School of Science, Westlake University, Hangzhou, Zhejiang Province 310030, China*

†Electronic supplementary information (ESI) available: Full descriptions of experimental methods, crystal structures, PXRD patterns, ICP-AES results, EDS mapping, and EPR characterization results and analysis. See DOI: https://doi.org/10.1039/d4qi02324b

that tuning the electronic configurations and coordination environments of lanthanide ions could enforce electron spins with s-orbital characteristics and strong hyperfine coupling.[30–33] These features give rise to weak spin–orbit coupling and clock-like states, respectively, which improve the qubit performance including T_1 and T_2.

So far, only two lanthanide-based MOFs (Ln-MOFs) have been demonstrated to behave as qubits.[34,35] Both consist of Gd^{3+} ions that exhibit spin coherence well above 10 K, which was attributed to the weak spin–orbit coupling of Gd^{3+}. However, the qubit performance of other lanthanide ions in MOFs has not been investigated, and its optimization strategies await elucidation. Herein, we report two new MOFs embedding lanthanide qubits that were synthesized by doping Nd^{3+} and Gd^{3+} into $[N(C_2H_5)_4][La(CAN)_2(H_2O)]$ (CAN^{2-} = chloranilate). The anisotropic $4f^3$ electron configuration of Nd^{3+} gives rise to a strong spin–orbit coupling and a low ground spin state (S = 3/2), whereas the spherically symmetric $4f^7$ electron configuration of Gd^{3+} leads to a weak spin–orbit coupling and a high ground spin state (S = 7/2). By examining the spin dynamics of these two materials at various temperatures and doping levels by pulse electron paramagnetic resonance (EPR) spectroscopy, we elaborated their spin relaxation and decoherence mechanisms to show that the low spin concentration, weak spin–orbit coupling, and low ground spin state help improve the qubit performance.

Results and discussion

Structures and synthesis

$[N(C_2H_5)_4][La(CAN)_2(H_2O)]$ (La(CAN)), $[N(C_2H_5)_4][Nd(CAN)_2(H_2O)]$ (Nd(CAN)), and $[N(C_2H_5)_4][Gd(CAN)_2]$ (Gd(CAN)) exhibit layered structures in which lanthanide ions and CAN^{2-} ligands form anionic square lattices separated by $N(C_2H_5)_4^+$ cations (Fig. S1–S3†).[36,37] The interlayer distances are approximately 1 nm. La(CAN) and Nd(CAN) are isostructural where La^{3+} and Nd^{3+} display a 9-coordinated capped square antiprismatic geometry composed of four bidentate CAN^{2-} ligands and a H_2O molecule (Fig. 1c and d). In contrast, Gd^{3+} in Gd(CAN) exhibits an 8-coordinated square antiprismatic geometry without coordinating H_2O (Fig. 1e).

Based on the literature, we synthesized La(CAN), Nd(CAN), and Gd(CAN) by heating $Ln(NO_3)_3$ (Ln^{3+} = La^{3+}, Nd^{3+}, and Gd^{3+}), chloranilic acid, and $[N(C_2H_5)_4]Cl$ in a mixture of *N*,*N*-dimethylformamide (DMF) and H_2O at 130 °C for 16 h.[36] Powder X-ray diffraction (PXRD) confirmed their structures and crystallinity (Fig. S4†). We further synthesized magnetically diluted MOFs, $[N(C_2H_5)_4][Nd_{x/100}La_{1-x/100}(CAN)_2(H_2O)]$ (x = 0.5, 1, 4, and 20; abbreviated as $\mathbf{Nd_xLa_{100-x}}$) and $[N(C_2H_5)_4][Gd_{y/100}La_{1-y/100}(CAN)_2(H_2O)_{1-y/100}]$ (y = 0.1, 0.5, 1, and 20; abbreviated as $\mathbf{Gd_yLa_{100-y}}$), using the same procedures with various stoichiometric ratios between Nd^{3+} (or Gd^{3+}) and La^{3+} (Fig. 1a and b). PXRD characterization of the doped samples confirmed that doping does not change the structure of the matrix, La(CAN) (Fig. S5†). Inductively coupled plasma atomic emission spectroscopy (ICP-AES) revealed that the actual doping levels of Nd^{3+} and Gd^{3+} are consistent with the designated values (Table S1†). The spatial distributions of these dopants are homogeneous as evidenced by the energy dispersive X-ray spectroscopy (EDS) mapping of $\mathbf{Nd_{20}La_{80}}$ and $\mathbf{Gd_{20}La_{80}}$ (Fig. S6 and S7†).

Continuous wave (CW) EPR spectroscopy

We conducted X-band (9.6 GHz) CW EPR spectroscopic characterization of $\mathbf{Nd_4La_{96}}$ and $\mathbf{Gd_1La_{99}}$ at 8 K and 90 K, respectively. The CW EPR spectrum of $\mathbf{Nd_4La_{96}}$ shows obvious rhombic signals indicating g-anisotropy (Fig. 2a). It can be fitted with the following spin Hamiltonian:

$$\hat{H} = \mu_B \boldsymbol{B}^T \boldsymbol{g} \hat{\boldsymbol{S}} + \hat{\boldsymbol{S}}^T \boldsymbol{A} \hat{\boldsymbol{I}} \quad (1)$$

where $\boldsymbol{g}$ represents the g-tensor, $\boldsymbol{A}$ represents the hyperfine coupling tensor, $\boldsymbol{B}$ represents the magnetic field, $\hat{\boldsymbol{S}}$ represents the electron spin operator, $\hat{\boldsymbol{I}}$ represents the nuclear spin operator, and μ_B represents the Bohr magneton. The first term describes the Zeeman splitting of the electron spin, and the second term describes the hyperfine interaction between the electron spin and nuclear spin of Nd^{3+}. The latter is only relevant for isotopes with non-zero nuclear spins (I = 7/2 for ^{143}Nd and ^{145}Nd with 12.2% and 8.3% natural abundance, respectively). Because hyperfine splitting is not well resolved in y and z directions, A_y and A_z are not included in the fitting. The spectrum can be well reproduced with S = 1/2, g_x = 3.54, g_y = 2.59, and g_z = 1.09 for all isotopes and A_x = 1237 MHz for ^{143}Nd and ^{145}Nd. Thus, the strong spin–orbit coupling of Nd^{3+} causes significant g-anisotropy and large zero-field splitting, the latter of which makes Nd^{3+} embedded in La(CAN) behaving as an effective S = 1/2 spin system. This is consistent with previous studies on Nd^{3+} in other materials.[38] The small features at approximately 482 mT that cannot be fitted using eqn (1) may originate from the polycrystalline effect.[38,39]

The CW EPR spectrum of $\mathbf{Gd_1La_{99}}$ is shown in Fig. 2b. It can be fitted with the following spin Hamiltonian:

$$\begin{aligned}\hat{H} = {} & g_{iso}\mu_B \boldsymbol{B}^T \cdot \hat{\boldsymbol{S}} + D\left[\hat{S}_Z^{\,2} - \frac{1}{3}S(S+1)\right] \\ & + E\left(\hat{S}_x^{\,2} - \hat{S}_y^{\,2}\right) + B_4^0\,\hat{O}_4^0 + B_4^2\,\hat{O}_4^2 + B_4^4\,\hat{O}_4^4\end{aligned} \quad (2)$$

where the first term represents the Zeeman splitting of electron spin with an isotropic g-factor, the second and third represent the second-order zero-field splitting with D and E as principal values, and the last three represent the fourth-order zero-field splitting ($\hat{O}_4^0$, $\hat{O}_4^2$, and $\hat{O}_4^4$ are the extended Stevens operators; B_4^0, B_4^2, and B_4^4 are the associated coefficients).[35,40] Fitting revealed S = 7/2, g_{iso} = 2.007, D = 339 MHz, E = 102 MHz, B_4^0 = −0.27 MHz, B_4^2 = 12.7 MHz, and B_4^4 = 10.8 MHz. Both the g-isotropy and small zero field splitting parameters indicate weak magnetic anisotropy of Gd^{3+} embedded in La(CAN) due to its weak spin–orbit coupling.

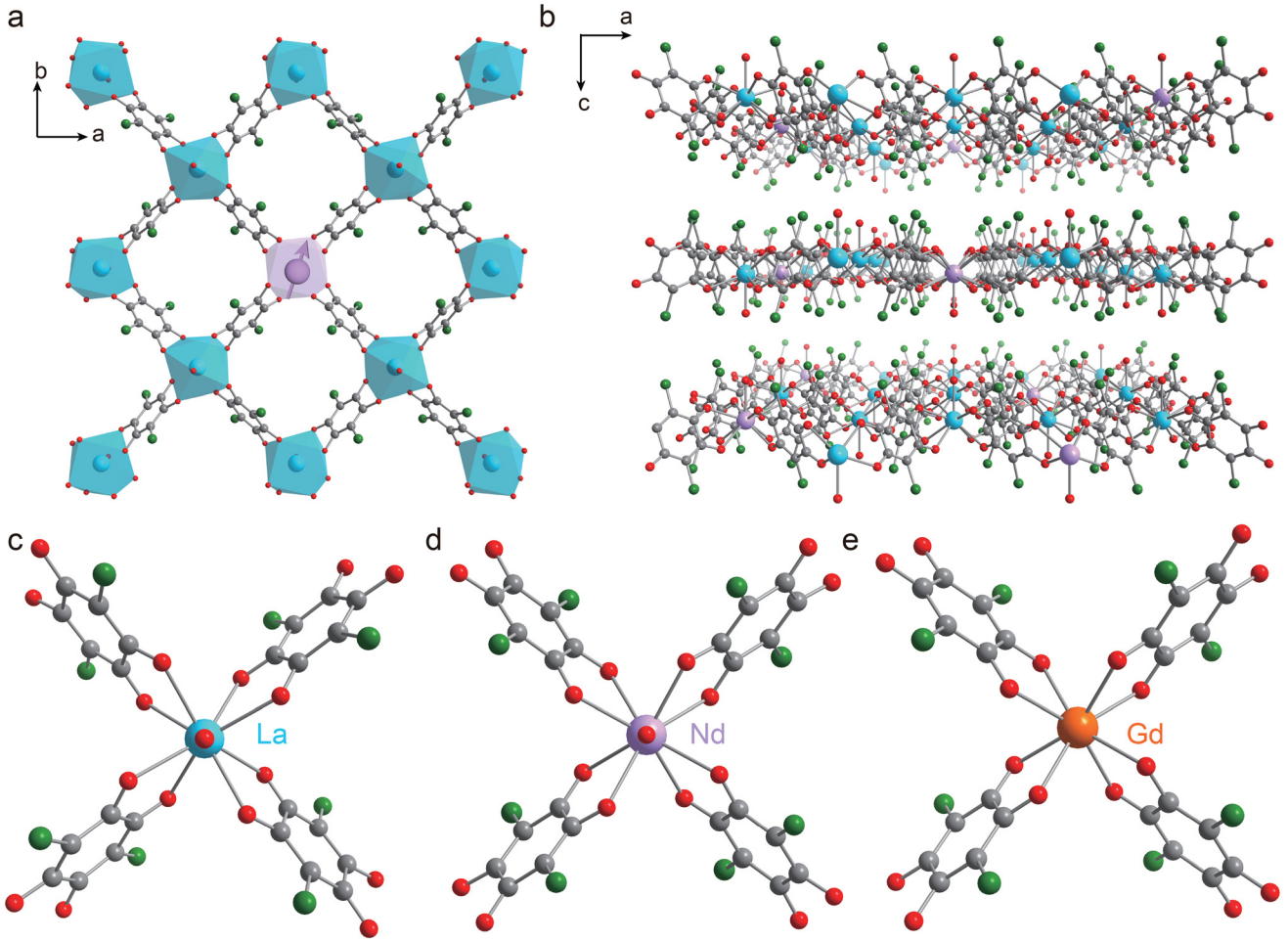

Fig. 1 (a) Portions of the crystal structure viewed along the crystallographic *c* axis and (b) the crystallographic *b* axis for magnetically diluted MOFs exemplified by $\mathbf{Nd_xLa_{100-x}}$. (c–e) Coordination environments of La^{3+}, Nd^{3+}, and Gd^{3+}. Gray, red, green, cyan, purple, and orange spheres represent C, O, Cl, La, Nd, and Gd atoms, respectively. Hydrogen atoms and $N(C_2H_5)_4^+$ cations are omitted for clarity.

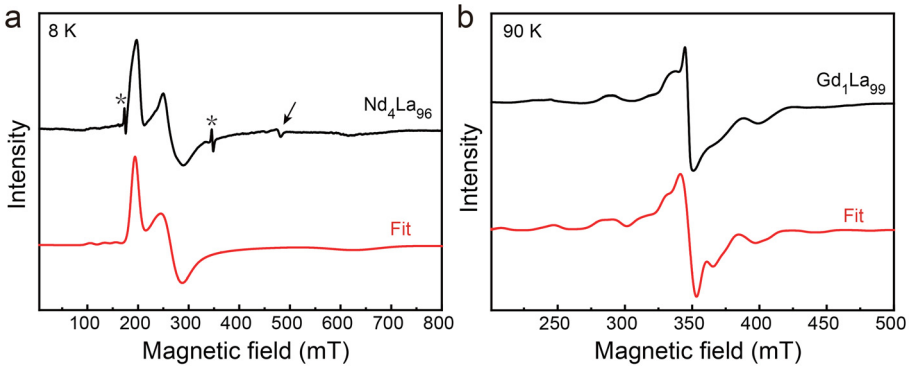

Fig. 2 X-band CW EPR spectra of (a) $\mathbf{Nd_4La_{96}}$ and (b) $\mathbf{Gd_1La_{99}}$ acquired at 8 K and 90 K, respectively. Red lines are fitting curves obtained using EasySpin.[60] Background signals of the resonator are marked with asterisks (Fig. S8†). The signal marked with an arrow is attributed to the polycrystallinity effect.[38,39]

Qubit behaviors

DiVincenzo's criteria dictate that a qubit should be a coherently addressable two-level quantum system.[4] We conducted X-band (9.6 GHz) pulse EPR spectroscopy to investigate the qubit behaviors and spin dynamics of $\mathbf{Nd_xLa_{100-x}}$ (x = 0.5, 1, and 4) and $\mathbf{Gd_yLa_{100-y}}$ (y = 0.1, 0.5, and 1). Echo-detected field sweep (EDFS)

spectra of these samples are consistent with their CW EPR spectra (Fig. S9a and S10†). We performed the following experiments under the magnetic field corresponding to g = 2.60 (B = 264.5 mT) and g = 1.99 (B = 347.4 mT) for Nd^{3+}- and Gd^{3+}-based samples, respectively, where EDFS spectra display maximum intensities. The T_1 and phase memory time (T_m), the latter of which involves all dephasing factors and resembles T_2, were characterized by picket-fence saturation recovery and Hahn echo decay pulse sequences, respectively (Fig. S9a and c†). All samples exhibit quantum coherence at 3.2 K or 3.4 K (Fig. 3a, b, d and e).

To verify the coherent addressability of Nd^{3+} and Gd^{3+} in the La(CAN) matrix, we performed nutation experiments for $\mathbf{Nd_{0.5}La_{99.5}}$ and $\mathbf{Gd_{0.1}La_{99.9}}$ at 5.2 K and 30 K, respectively, at various microwave powers (Fig. S9b†). Rabi oscillations clearly manifest themselves in the time-domain nutation curves (Fig. 3c and f), whose Fourier transforms display two peaks (Fig. S11a and c†). One of the peaks is independent of the microwave power: it remains at 11.7 MHz for $\mathbf{Nd_{0.5}La_{99.5}}$ and 14.6 MHz for $\mathbf{Gd_{0.1}La_{99.9}}$. Accordingly, this peak is attributed to the Larmor frequency of ^{1}H nuclear spin as a manifestation of the Hartmann–Hahn effect.[41] The other peak exhibits a linear relationship with the microwave magnetic field strength, which is attributed to the Rabi frequency (Fig. S11b and d†).[42] Therefore, the electron spins of $\mathbf{Nd_xLa_{100-x}}$ and $\mathbf{Gd_yLa_{100-y}}$ can be coherently manipulated to form arbitrary superpositions of their constituent states, thereby behaving as qubits.

Spin relaxation

Spin relaxation requires energy exchange between the target electron spin and the environment, which is mediated by the surrounding phonon bath and spin bath. The spin–phonon coupling gives rise to spin–lattice relaxation, which may undergo various mechanisms that exhibit different temperature dependencies yet are independent of the spin concentration.[43] In contrast, the spin–spin dipolar coupling induces relaxation through spin flip-flop, giving rise to cross relaxation that is typically concentration-dependent.[44,45] Hence, investigating spin relaxation at various temperatures and spin concentrations could distinguish the contributions of spin–phonon coupling and spin–spin dipolar coupling.

The T_1 of $\mathbf{Nd_xLa_{100-x}}$ was measurable below 8.0 K (Fig. S12–S15 and Table S6†). As shown in Fig. 4a, it decreases sharply with an increase in temperature for each sample. For instance, $\mathbf{Nd_{0.5}La_{99.5}}$ exhibits a T_1 value of 924 μs at 3.4 K, which drops to 1.48 μs at 8.0 K. Meanwhile, T_1 is weakly dependent on the spin concentration (Fig. 3a and 4a). $\mathbf{Nd_{0.5}La_{99.5}}$ and $\mathbf{Nd_1La_{99}}$ display almost identical T_1 values across the temperature range of 3.4 K–8.0 K. Their temperature (T) dependence of T_1 obeys $1/T_1 \propto T^7$, which is consistent with the Raman relaxation process involving acoustic phonons (Fig. 4b).[46] This relationship is valid when the Debye temperature (T_D), *i.e.* the temperature corresponding to the

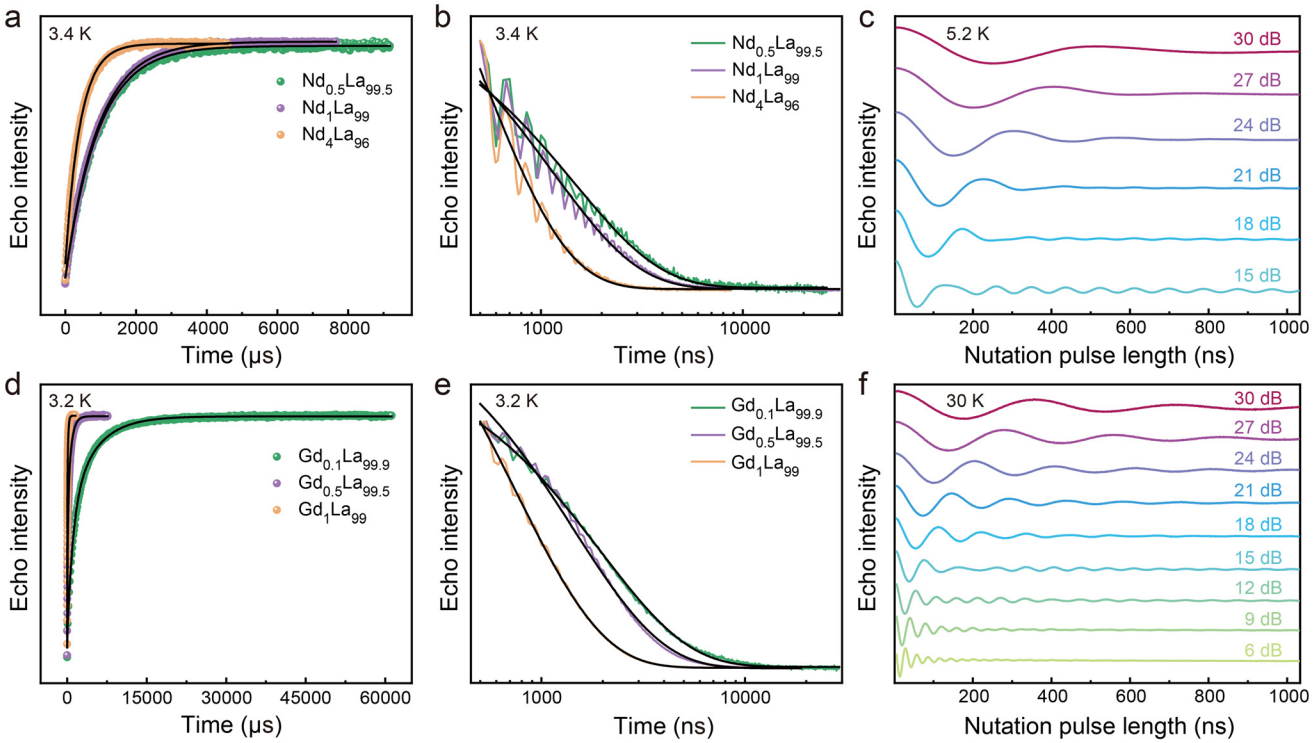

Fig. 3 (a) Saturation recovery curves and (b) Hahn echo decay curves of $\mathbf{Nd_xLa_{100-x}}$ collected at 3.4 K. (c) Nutation curves of $\mathbf{Nd_{0.5}La_{99.5}}$ collected under various microwave attenuations at 5.2 K. (d) Saturation recovery curves and (e) Hahn echo decay curves of $\mathbf{Gd_yLa_{100-y}}$ collected at 3.2 K. (f) Nutation curves of $\mathbf{Gd_{0.1}La_{99.9}}$ collected under various microwave attenuations at 30 K. Black lines in (a), (b) and (e) are mono-exponential decay fitting curves and those in (d) are bi-exponential decay fitting curves.

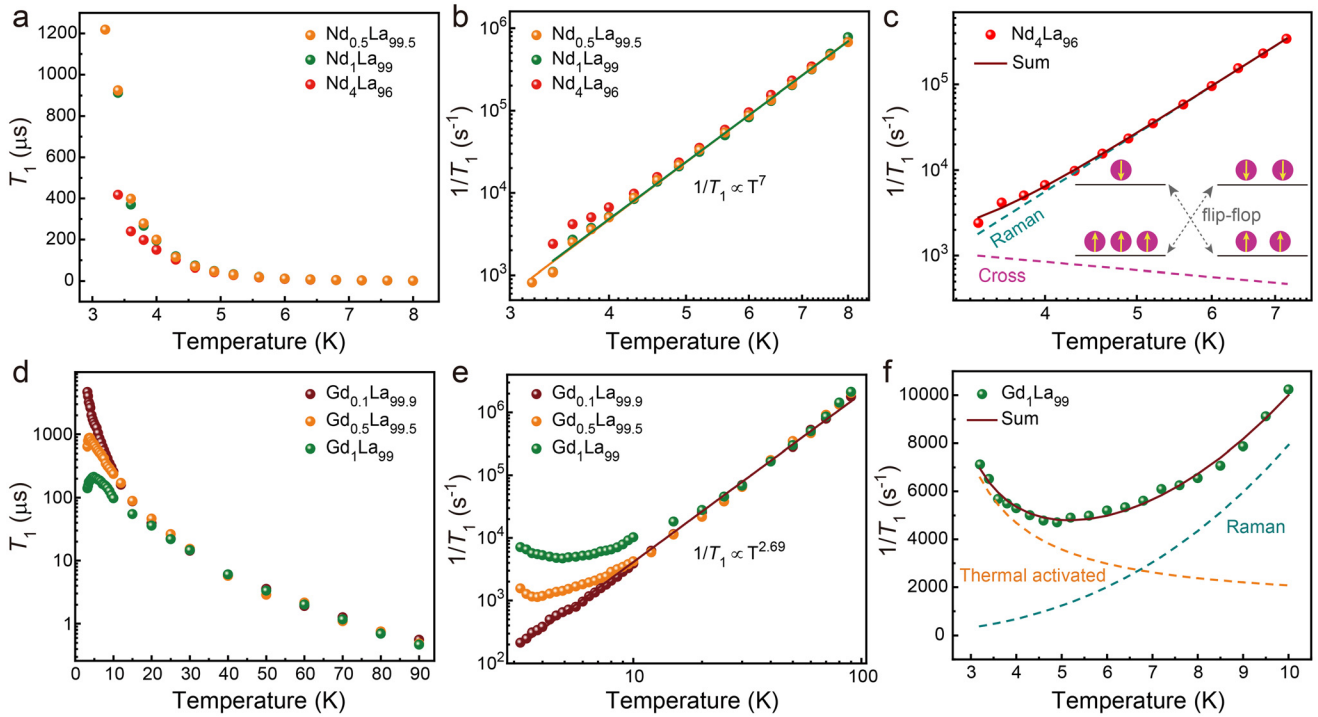

Fig. 4 (a and b) T_1 and $1/T_1$ *vs.* T data for $\mathbf{Nd_xLa_{100-x}}$. Orange and green lines are fits to the data by $1/T_1 = A_{\mathrm{Raman}}T^7$ for $\mathbf{Nd_{0.5}La_{99.5}}$ and $\mathbf{Nd_1La_{99}}$, respectively. (c) Fitting of $1/T_1$ *vs.* T data for $\mathbf{Nd_4La_{96}}$ with eqn (3). Turquoise and violet-red dashed lines represent contributions from Raman and cross relaxation, respectively, and the wine solid line is their sum. The inset illustrates the cross relaxation caused by flip-flop between saturated spins (right) and nearby thermally populated spins (left). (d and e) T_1 and $1/T_1$ *vs.* T data for $\mathbf{Gd_yLa_{100-y}}$. The wine line is the fit to the data by $1/T_1 = A_{\mathrm{Raman}}T^{2.69}$ for $\mathbf{Gd_{0.1}La_{99.9}}$. (f) Fitting of $1/T_1$ *vs.* T data for $\mathbf{Gd_1La_{99}}$ with eqn (4). Turquoise and orange dashed lines represent contributions from the Raman and thermally activated relaxation, respectively, and the wine solid line is their sum.

cutoff frequency of acoustic phonons, is much higher than the experimental temperature (Fig. S16; see the detailed discussion in Note S1†). Indeed, through simulation, we found $T_D > 80$ K for these two materials. This value is comparable with the T_D observed for lanthanide ions in inorganic solids, *e.g.* Yb-doped Y_2SiO_5 ($T_D = 100$ K), indicating a rigid lattice of the MOF matrix.[47]

$\mathbf{Nd_4La_{96}}$ exhibits a shorter T_1 value than those of $\mathbf{Nd_{0.5}La_{99.5}}$ and $\mathbf{Nd_1La_{99}}$: its T_1 is 417 μs at 3.4 K and it drops to 2.93 μs at 7.2 K (Fig. 4a). The temperature dependence of T_1 slightly deviates from $1/T_1 \propto T^7$ below 4 K (Fig. 4b). Because this deviation only occurs in the sample with a high doping level, it is likely a manifestation of the cross relaxation rather than the direct process—the former is dependent on the spin concentration yet the latter is not.[43] To understand this behavior, we propose a model to describe the cross relaxation taking place in the saturation recovery experiment. It accounts for flip-flop events between saturated spins and adjacent thermally populated spins (Fig. 4c inset). The flip-flop rate scales with the spin–spin dipolar coupling strength, which becomes salient at high spin concentrations.[48] For Nd^{3+} that behaves as a pseudo $S = 1/2$ spin system, this model gives rise to a cross relaxation rate that is proportional to the Boltzmann population difference between ground and excited spin sublevels (see the detailed discussion in Note S2†). Accordingly, we fitted the temperature dependence of the T_1 value of $\mathbf{Nd_4La_{96}}$ with the following equation:

$$\frac{1}{T_1} = A_{\mathrm{cross}}\frac{1-\exp(-h\nu/k_BT)}{1+\exp(-h\nu/k_BT)} + A_{\mathrm{Raman}}T^7 \qquad (3)$$

where A_{cross} and A_{Raman} represent pre-factors of cross relaxation and Raman relaxation, respectively, h represents the Planck constant, ν represents the Larmor frequency of the electron spin, and k_B represents the Boltzmann constant. As shown in Fig. 4c, the cross relaxation rate is significantly smaller than the Raman relaxation rate. Thus, both spin–phonon coupling and spin–spin dipolar coupling contribute to spin relaxation in $\mathbf{Nd_xLa_{100-x}}$ with the former being dominant.

$\mathbf{Gd_yLa_{100-y}}$ samples show measurable T_1 values for up to 90 K (Fig. S12, S17–S19 and Tables S7–S9†). The T_1 value of $\mathbf{Gd_{0.1}La_{99.9}}$ decreases monotonically with an increase in temperature: it drops from 4.68 ms at 3.2 K to 0.56 μs at 90 K (Fig. 4d). The temperature dependence of T_1 shows a Raman-like relaxation process with $1/T_1 \propto T^{2.69}$ (Fig. 4e). This small exponent value indicates the participation of both acoustic and optical phonons in Raman relaxation,[46,49] and it is consistent with previously reported values for Gd^{3+}-based spin systems.[50] $\mathbf{Gd_{0.5}La_{99.5}}$ and $\mathbf{Gd_1La_{99}}$ show comparable T_1 values and relaxation behaviors with those of $\mathbf{Gd_{0.1}La_{99.9}}$ above 10 K

and 20 K, respectively (Fig. 4d and e). Below these temperatures, T_1 decreases with an increase in spin concentration. At 3.2 K, T_1 drops to 640 μs and 141 μs for samples with 0.5% and 1% doping levels, respectively. These results show that both spin–phonon coupling and spin–spin dipolar coupling contribute to the spin relaxation of $\mathbf{Gd_yLa_{100-y}}$. In the high-temperature region, spin–phonon coupling dominates regardless of the spin concentration, whereas in the low-temperature region, spin–spin dipolar coupling is salient at a high spin concentration.

Notably, $\mathbf{Gd_{0.5}La_{99.5}}$ and $\mathbf{Gd_1La_{99}}$ exhibit reciprocating thermal behaviors below 3.8 K and 4.9 K, respectively, where their T_1 values decrease with a decrease in temperature (Fig. 4d). For instance, upon cooling $\mathbf{Gd_1La_{99}}$, its T_1 increases from 98 μs at 10 K to 213 μs at 4.9 K, and it then decreases to 141 μs at 3.2 K. This trend indicates the presence of a thermally activated relaxation process that reaches the maximum rate below 3.2 K.[43] Hence, we fitted this trend using the following equation:

$$\frac{1}{T_1} = A_{\text{thermal}} \exp\left(\frac{E_a}{k_B T}\right) + A_{\text{Raman}} T^n \quad (4)$$

where A_{thermal} and E_a are the pre-factor and activation energy of thermally activated relaxation, respectively, and n is the exponent of Raman relaxation (Fig. 4f). n was fixed at 2.69 based on the observation from $\mathbf{Gd_{0.1}La_{99.9}}$. Fitting revealed that spin relaxation below 6.5 K is dominated by thermally activated relaxation with E_a = 0.47 meV, which corresponds to a temperature of 5.4 K.

Such reciprocating thermal behavior has been observed in another Gd^{3+}-based MOF and several single ion magnets whose magnetic relaxation times, acquired by alternative current susceptibility measurements, become shorter at a lower temperature.[51,52] To our knowledge, it has not been observed previously in spin relaxation probed by pulse EPR spectroscopy. This phenomenon was attributed to the phonon bottleneck effect, but its physical interpretation is still unclear.[51,52] Our experiments showed that it involves thermal activation and becomes more salient at a higher spin concentration, so we tentatively assign it as a manifestation of spin–spin dipolar coupling and may be related to electron spin flip-flop involving multiple spin sublevels. We will investigate the nature of the reciprocating thermal behavior of $\mathbf{Gd_yLa_{100-y}}$ in future studies.

Spin decoherence

In theory, T_m may reach $2T_1$ (Fig. 5g), but it is typically much shorter than T_1 in molecular systems due to other dephasing processes induced by environmental magnetic noise, *e.g.* nearby electron spins and nuclear spins, through instantaneous diffusion (ID) and spectral diffusion (SD).[53] ID is caused by instantaneous spin rotation during the pulse (Fig. 5k). It scales with the spin concentration but is inherently independent of temperature. The SD takes place during the free evolution time of a pulse sequence. It mainly involves three kinds of events for lanthanide qubits: relaxation-induced stochastic flipping of nearby electron spins (electronic SD, Fig. 5h), direct/indirect electron spin flip-flop (Fig. 5i), and nuclear spin flip-flop (nuclear SD, Fig. 5j).[48] The nuclear SD is independent of both temperature and electron spin concentration, while the former two are concentration-dependent. The rate of electronic SD scales with $1/\sqrt{T_1}$ that is temperature-dependent,[47,54] whereas the rate of electron spin flip-flop is nearly temperature-independent for Nd^{3+} and Gd^{3+} under our experimental conditions (Fig. S20; see the detailed discussion in Note S3†).[48,55] Thus, conducting variable-temperature and variable-concentration T_m measurements would reveal spin decoherence mechanisms.

We conducted Hahn echo decay experiments with various pulse lengths (32 ns, 64 ns, and 128 ns for the π pulse) to articulate the contribution of ID, which should decrease with an increase in pulse lengths.[48] While long and selective pulses do not alter the T_m of $\mathbf{Nd_{0.5}La_{99.5}}$ and $\mathbf{Gd_{0.1}La_{99.9}}$, they significantly improve the T_m of $\mathbf{Nd_4La_{96}}$ and $\mathbf{Gd_1La_{99}}$ and the associated improvements decrease with an increase in temperature (Fig. S21 and S22†). Therefore, ID is negligible at low spin concentrations, whereas it becomes significant at high spin concentrations. In addition, the Hahn echo intensity displays oscillations with the free evolution time, indicating electronic spin echo envelope modulation (ESEEM) from nearby nuclear spins (Fig. 3b and e). Combination-peak ESEEM measurements (Fig. S9d†) of $\mathbf{Nd_{0.5}La_{99.5}}$ and $\mathbf{Gd_{0.1}La_{99.9}}$ revealed modulation frequencies signifying nuclear spins of ^{1}H, ^{13}C, and ^{139}La (Fig. S23†). Hence, these nuclear spins are coupled with the electron spin of Nd^{3+} or Gd^{3+}, causing decoherence through nuclear SD.

In the following analysis, we focused on the T_m acquired with the π pulse being 32 ns with the shot repetition time being greater than $5T_1$ (see the detailed discussion in Note S4; Fig. S24 and S25, Tables S2 and S3†). The obtained Hahn echo decay curves were fitted by mono-exponential decay function (see the detailed discussion in Note S5; Fig. S26–S33, Table S4†). It decreases with an increase in temperature and an increase in spin concentration for both Nd^{3+} and Gd^{3+} (Fig. 5a and d; Fig. S34–S40, Tables S6–S9†). For instance, the T_m of $\mathbf{Nd_{0.5}La_{99.5}}$ drops from 1.46 μs at 3.4 K to 0.28 μs at 8.0 K, and increasing the doping level to 4% reduces the T_m to 0.49 μs at 3.4 K. To understand the decoherence sources, we analyzed the T_m of $\mathbf{Nd_xLa_{100-x}}$ with the following equation:

$$\frac{1}{T_m} = \frac{1}{2T_1} + A_{\text{SD,e}} \frac{1}{\sqrt{T_1}} + C \quad (5)$$

where the second term describes decoherence caused by the electronic SD, and the last term is a temperature-independent constant that encompasses contributions from the electron spin flip-flop, nuclear SD, and ID. Fitting the temperature dependencies of the T_m of $\mathbf{Nd_xLa_{100-x}}$ with eqn (5) revealed that the electronic SD dominates for all doping levels, whereas C increases significantly with an increase in the spin concentration possibly due to enhanced ID or electron spin flip-flop (Fig. 5b and c; Fig. S41a, Table S5†). Hence, the spin coherence of Nd^{3+} is mainly limited by relaxation-induced spectral

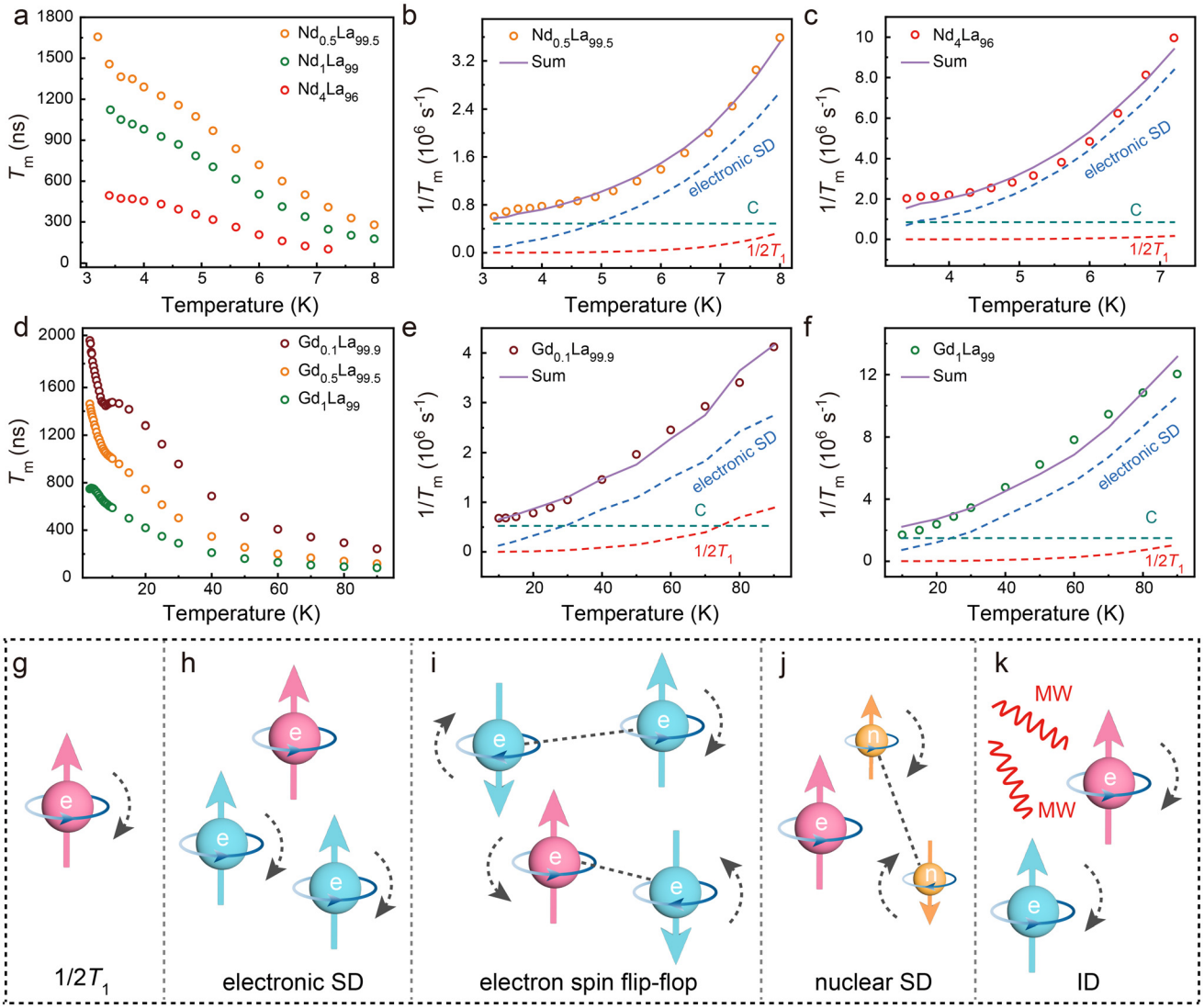

Fig. 5 (a and d) T_m *vs.* T data for $\mathbf{Nd_xLa_{100-x}}$ and $\mathbf{Gd_yLa_{100-y}}$. (b, c, e and f) Fitting of $1/T_m$ *vs.* T data for $\mathbf{Nd_{0.5}La_{99.5}}$, $\mathbf{Nd_4La_{96}}$, $\mathbf{Gd_{0.1}La_{99.9}}$, and $\mathbf{Gd_1La_{99}}$ with eqn (5). Red, blue, and green dashed lines represent contributions from spin relaxation, electronic SD, and a temperature-independent constant, C, which encompasses contributions from electron spin flip-flop, nuclear SD, and ID. The plum solid line is their sum. (g–k) Spin decoherence mechanisms:[48] (g) spin relaxation (1/2T_1); (h) electronic SD; (i) direct/indirect electron spin flip-flop; (j) nuclear SD; (k) ID. The pink, cyan, and orange spheres represent the electron spin of interest, the neighbouring electron spin causing decoherence, and the neighbouring nuclear spins, respectively. MW represents microwave. Dashed lines represent dipolar coupling between spins and dashed arrows describe spin flipping events.

diffusion, and reducing the doping level of Nd^{3+} improves its T_m.

Above 10 K, $\mathbf{Gd_yLa_{100-y}}$ exhibits similar decoherence behaviors with $\mathbf{Nd_xLa_{100-x}}$ (Fig. 5d). Analyzing the T_m in the temperature range of 10 K–90 K with eqn (5) revealed the dominant role of electronic SD in decoherence (Fig. 5e and f; Fig. S41b, Table S5†). Below 10 K, the T_m of Gd^{3+} decreases with an increase in the doping level, and it displays distinct temperature dependencies that cannot be fitted by eqn (5) (Fig. 5d). The T_m of $\mathbf{Gd_{0.1}La_{99.9}}$ and $\mathbf{Gd_{0.5}La_{99.5}}$ increases linearly with a decrease in temperature below 6.8 K and 6.4 K, respectively. Meanwhile, $\mathbf{Gd_{0.1}La_{99.9}}$ and $\mathbf{Gd_1La_{99}}$ exhibit plateaus of T_m at 6.8 K–12 K and 3.2 K–4.3 K, respectively. We note that the overall Zeeman splitting between $m_s = -7/2$ and $m_s = -7/2$ sublevels of Gd^{3+} is approximately 69 GHz, which corresponds to 3.3 K. Considering the comparability between these temperatures, the unique low-temperature decoherence behaviors may be related to the Boltzmann population of spin sublevels. In addition, the methyl tunnelling within $N(C_2H_5)_4^+$ cations in the pores of $\mathbf{Gd_yLa_{100-y}}$ may also contribute to the decoherence behaviors below 10 K.[56–58]

Strategies to improve the spin qubit performance of Ln-MOFs

The above analysis reveals critical roles of spin–phonon coupling and spin–spin dipolar coupling in the spin dynamics of $\mathbf{Nd_xLa_{100-x}}$ and $\mathbf{Gd_yLa_{100-y}}$ (Fig. 6a). The spin–phonon coupling causes Raman relaxation that dominates the spin relax-

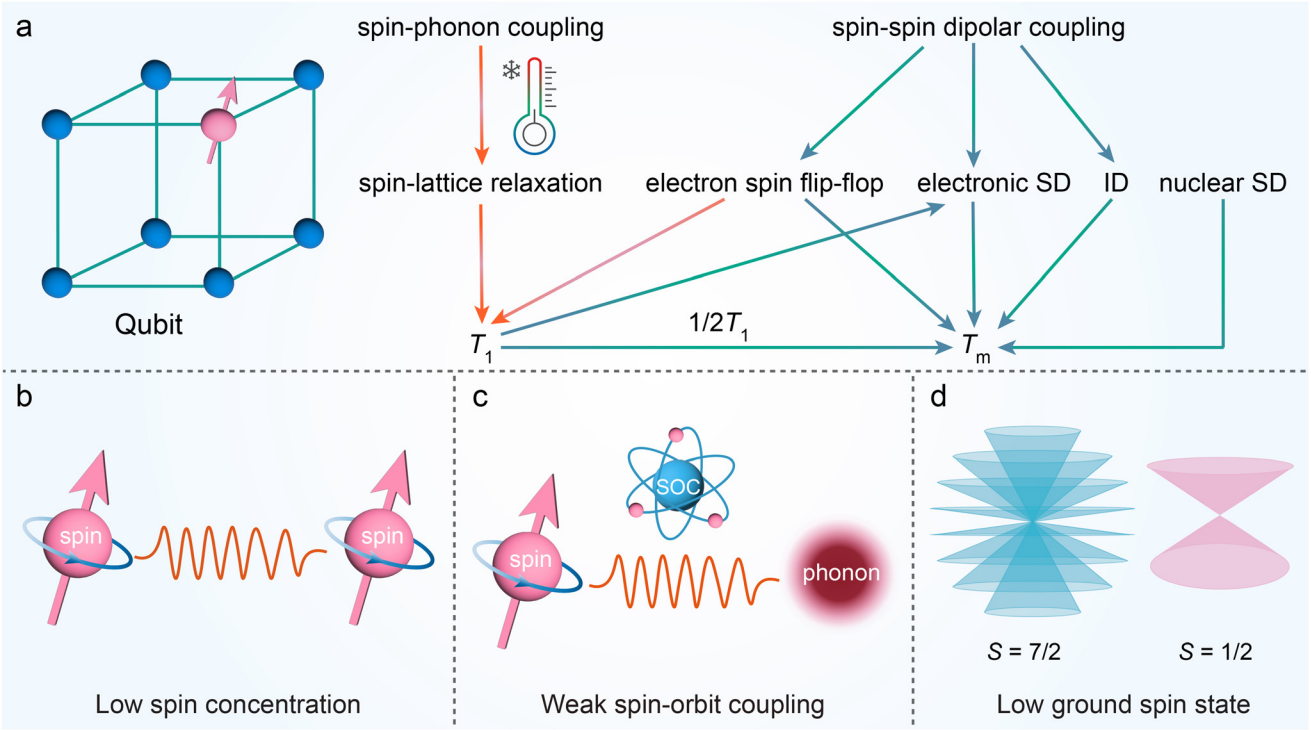

Fig. 6 (a) Spin relaxation and decoherence mechanisms of Ln-MOFs. Orange-red and blue-green arrows specify influences on T_1 and T_m, respectively. (b–d) Optimization strategies for the qubit performance of Ln-MOFs. The wavy line represents interaction. SD, ID, and SOC represent spectral diffusion, instantaneous diffusion, and spin–orbit coupling, respectively.

ation at relatively high temperatures for both materials. Meanwhile, relaxation-induced spectral diffusion (electronic SD) plays a major role in spin decoherence—although T_m is much shorter than T_1, it is indirectly limited by T_1. The spin–spin dipolar coupling causes decoherence through electronic SD, ID, and electron spin flip-flop, the latter of which also mediates cross relaxation. Our analysis of cross relaxation in T_1 measurements shows that its rate decreases with an increase in temperature, which might explain the unique reciprocating thermal behavior observed in $\mathbf{Gd_{0.5}La_{99.5}}$ and $\mathbf{Gd_1La_{99}}$. Overall, both spin–phonon coupling and spin–spin dipolar coupling should be suppressed to improve the key qubit metrics, *i.e.* T_1 and T_m, of Ln-MOFs.

Our experiments show that lanthanide qubits exhibit decent T_1 and T_m at low temperatures and spin concentrations (Fig. 6b). Lowering the temperature reduces the number of active phonons that couple with spins, thereby inhibiting spin–lattice relaxation. It also improves T_m by suppressing the electronic SD. Reducing the spin concentration weakens the spin–spin dipolar coupling. Therefore, diluting lanthanide ions in diamagnetic matrices could improve their T_1 and T_m.

Comparisons between $\mathbf{Nd_xLa_{100-x}}$ and $\mathbf{Gd_yLa_{100-y}}$ show that weakening the spin–orbit coupling and reducing the ground spin state also enhance the qubit performance (Fig. 6c and d). The spin–orbit coupling determines the strength of spin–phonon coupling.[59] The $4f^3$ electronic configuration of Nd^{3+} gives rise to a strong spin–orbit coupling. As a result, the T_1 of $\mathbf{Nd_xLa_{100-x}}$ declines sharply with an increase in temperature, limiting the operation temperature of these materials below 8 K. In contrast, Gd^{3+} displays weak spin–orbit coupling thanks to its spherically symmetric $4f^7$ electron configuration that quenches the orbital angular momentum. This prompts $\mathbf{Gd_yLa_{100-y}}$ to maintain quantum coherence for up to 90 K. On the other hand, lowering the ground spin state not only reduces the spin–spin dipolar coupling but also avoids decoherence from electron spin flip-flop through multiple spin sublevels. Therefore, to maximize the T_1 and T_m of Ln-MOFs, one should choose appropriate lanthanide ions and optimize their coordination environments to minimize both spin–orbit coupling and the ground spin state. Notably, this is contrary to the design principle of lanthanide-based single-molecule magnets, which demand large spin–orbit coupling to improve the magnetic anisotropy and high ground spin state to enlarge the spin reversal barrier.[22] Comparisons between the spin relaxation of lanthanide qubits and the magnetic relaxation of lanthanide-based single-molecule magnets would reveal insights into the opposite design principles of these systems.

Conclusions

In summary, we synthesized two solid-state lanthanide qubits by embedding Nd^{3+} and Gd^{3+} ions into a MOF. Through variable-temperature and variable-concentration spin dynamic

characterization of these materials, we articulated their spin relaxation and decoherence mechanisms that reflect the critical influences of the environmental phonon bath and spin bath. Spin–phonon coupling plays a major role in the spin relaxation of both Nd^{3+} and Gd^{3+}, and it indirectly limits the T_m through relaxation-induced spectral diffusion. Spin–spin dipolar coupling contributes to cross relaxation and participates in several spin decoherence processes including relaxation-induced spectral diffusion, direct/indirect electron spin flip-flop, and instantaneous diffusion. This analysis highlights the low spin concentration, weak spin–orbit coupling, and low ground spin state as optimization strategies for the T_1 and T_m of lanthanide qubits, providing guidelines for the design of Ln-MOFs as building units of quantum memories.

Author contributions

X. D. designed and conducted experiments. L. S. conceived the idea and oversaw the project. X. D. and L. S. analyzed the data and co-wrote the manuscript.

Data availability

The data supporting this article have been included as part of the ESI.†

Conflicts of interest

There are no conflicts to declare.

Acknowledgements

This work was supported by the National Natural Science Foundation of China (No. 22273078) and the Hangzhou Municipal Funding Team of Innovation (TD2022004). We thank Dr Luming Yang, Prof. Mircea Dincă, and Prof. Tijana Rajh for assistance with preliminary experiments and the Instrumentation and Service Center for Molecular Sciences and the Instrumentation and Service Center for Physical Sciences at Westlake University for facility support and technical assistance. X. D. thanks Danyu Gu and Lingyu Xiao for their support with pulse EPR and ICP-AES experiments and Haozhou Sun, Yi Yang, Weibin Ni, and Zhecheng Sun at Westlake University for helpful discussions.

References

1 N. Gisin and R. Thew, Quantum communication, *Nat. Photonics*, 2007, **1**, 165–171.
2 A. I. Lvovsky, B. C. Sanders and W. Tittel, Optical quantum memory, *Nat. Photonics*, 2009, **3**, 706–714.
3 N. Sangouard, C. Simon, H. de Riedmatten and N. Gisin, Quantum repeaters based on atomic ensembles and linear optics, *Rev. Mod. Phys.*, 2011, **83**, 33–80.
4 D. P. DiVincenzo, The physical implementation of quantum computation, *Fortschr. Phys.*, 2000, **48**, 771–783.
5 D. D. Awschalom, R. Hanson, J. Wrachtrup and B. B. Zhou, Quantum technologies with optically interfaced solid-state spins, *Nat. Photonics*, 2018, **12**, 516–527.
6 P. Siyushev, K. Xia, R. Reuter, M. Jamali, N. Zhao, N. Yang, C. Duan, N. Kukharchyk, A. D. Wieck, R. Kolesov and J. Wrachtrup, Coherent properties of single rare-earth spin qubits, *Nat. Commun.*, 2014, **5**, 3895.
7 T. Zhong, J. M. Kindem, J. G. Bartholomew, J. Rochman, I. Craiciu, E. Miyazono, M. Bettinelli, E. Cavalli, V. Verma, S. W. Nam, F. Marsili, M. D. Shaw, A. D. Beyer and A. Faraon, Nanophotonic rare-earth quantum memory with optically controlled retrieval, *Science*, 2017, **357**, 1392–1395.
8 A. Seri, A. Lenhard, D. Rieländer, M. Gündoğan, P. M. Ledingham, M. Mazzera and H. de Riedmatten, Quantum correlations between single telecom photons and a multimode on-demand solid-state quantum memory, *Phys. Rev. X*, 2017, **7**, 021028.
9 I. Craiciu, M. Lei, J. Rochman, J. M. Kindem, J. G. Bartholomew, E. Miyazono, T. Zhong, N. Sinclair and A. Faraon, Nanophotonic quantum storage at telecommunication wavelength, *Phys. Rev. Appl.*, 2019, **12**, 024062.
10 M. Businger, A. Tiranov, K. T. Kaczmarek, S. Welinski, Z. Zhang, A. Ferrier, P. Goldner and M. Afzelius, Optical spin-wave storage in a solid-state hybridized electron-nuclear spin ensemble, *Phys. Rev. Lett.*, 2020, **124**, 053606.
11 A. Ortu, A. Holzäpfel, J. Etesse and M. Afzelius, Storage of photonic time-bin qubits for up to 20 ms in a rare-earth doped crystal, *npj Quantum Inf.*, 2022, **8**, 29.
12 J. Alexander, G. Dold, O. W. Kennedy, M. Šimėnas, J. O'Sullivan, C. W. Zollitsch, S. Welinski, A. Ferrier, E. Lafitte-Houssat, T. Lindström, P. Goldner and J. J. L. Morton, Coherent spin dynamics of rare-earth doped crystals in the high-cooperativity regime, *Phys. Rev. B*, 2022, **106**, 245416.
13 S. Gupta, X. Wu, H. Zhang, J. Yang and T. Zhong, Robust millisecond coherence times of erbium electron spins, *Phys. Rev. Appl.*, 2023, **19**, 044029.
14 Z. Q. Zhou, C. Liu, C. F. Li, G. C. Guo, D. Oblak, M. Lei, A. Faraon, M. Mazzera and H. de Riedmatten, Photonic integrated quantum memory in rare-earth doped solids, *Laser Photonics Rev.*, 2023, **17**, 2300257.
15 Y. Ma, Y.-Z. Ma, Z.-Q. Zhou, C.-F. Li and G.-C. Guo, One-hour coherent optical storage in an atomic frequency comb memory, *Nat. Commun.*, 2021, **12**, 2381.
16 M. Guo, S. Liu, W. Sun, M. Ren, F. Wang and M. Zhong, Rare-earth quantum memories: The experimental status quo, *Front. Phys.*, 2023, **18**, 21303.
17 T. Zhong and P. Goldner, Emerging rare-earth doped material platforms for quantum nanophotonics, *Nanophotonics*, 2019, **8**, 2003–2015.

18 J. M. Kindem, A. Ruskuc, J. G. Bartholomew, J. Rochman, Y. Q. Huan and A. Faraon, Control and single-shot readout of an ion embedded in a nanophotonic cavity, *Nature*, 2020, **580**, 201–204.
19 K. S. Pedersen, A.-M. Ariciu, S. McAdams, H. Weihe, J. Bendix, F. Tuna and S. Piligkos, Toward molecular 4f single-ion magnet qubits, *J. Am. Chem. Soc.*, 2016, **138**, 5801–5804.
20 J. G. C. Kragskow, J. Marbey, C. D. Buch, J. Nehrkorn, M. Ozerov, S. Piligkos, S. Hill and N. F. Chilton, Analysis of vibronic coupling in a 4f molecular magnet with FIRMS, *Nat. Commun.*, 2022, **13**, 825.
21 L. Escalera-Moreno, J. J. Baldoví, A. Gaita-Ariño and E. Coronado, Spin states, vibrations and spin relaxation in molecular nanomagnets and spin qubits: a critical perspective, *Chem. Sci.*, 2018, **9**, 3265–3275.
22 J. J. Baldoví, S. Cardona-Serra, J. M. Clemente-Juan, E. Coronado, A. Gaita-Ariño and A. Palii, Rational design of single-ion magnets and spin qubits based on mononuclear lanthanoid complexes, *Inorg. Chem.*, 2012, **51**, 12565–12574.
23 H.-C. Zhou, J. R. Long and O. M. Yaghi, Introduction to metal–organic frameworks, *Chem. Rev.*, 2012, **112**, 673–674.
24 H. Deng, S. Grunder, K. E. Cordova, C. Valente, H. Furukawa, M. Hmadeh, F. Gándara, A. C. Whalley, Z. Liu, S. Asahina, H. Kazumori, M. O'Keeffe, O. Terasaki, J. F. Stoddart and O. M. Yaghi, Large-pore apertures in a series of metal-organic frameworks, *Science*, 2012, **336**, 1018–1023.
25 T. Kamencek, N. Bedoya-Martínez and E. Zojer, Understanding phonon properties in isoreticular metal-organic frameworks from first principles, *Phys. Rev. Mater.*, 2019, **3**, 116003.
26 B. Yan, Lanthanide-functionalized metal–organic framework hybrid systems to create multiple luminescent centers for chemical sensing, *Acc. Chem. Res.*, 2017, **50**, 2789–2798.
27 F. Manna, M. Oggianu, N. Avarvari and M. L. Mercuri, Lanthanide-based metal–organic frameworks with single-molecule magnet properties, *Magnetochemistry*, 2023, **9**, 190.
28 C.-J. Yu, S. von Kugelgen, M. D. Krzyaniak, W. Ji, W. R. Dichtel, M. R. Wasielewski and D. E. Freedman, Spin and phonon design in modular arrays of molecular qubits, *Chem. Mater.*, 2020, **32**, 10200–10206.
29 J. M. Zadrozny, A. T. Gallagher, T. D. Harris and D. E. Freedman, A porous array of clock qubits, *J. Am. Chem. Soc.*, 2017, **139**, 7089–7094.
30 M. Shiddiq, D. Komijani, Y. Duan, A. Gaita-Ariño, E. Coronado and S. Hill, Enhancing coherence in molecular spin qubits via atomic clock transitions, *Nature*, 2016, **531**, 348–351.
31 K. Kundu, J. R. K. White, S. A. Moehring, J. M. Yu, J. W. Ziller, F. Furche, W. J. Evans and S. Hill, A 9.2 GHz clock transition in a Lu(II) molecular spin qubit arising from a 3,467 MHz hyperfine interaction, *Nat. Chem.*, 2022, **14**, 392–397.
32 R. Stewart, A. B. Canaj, S. Liu, E. R. Martí, A. Celmina, G. Nichol, H.-P. Cheng, M. Murrie and S. Hill, Engineering clock transitions in molecular lanthanide complexes, *J. Am. Chem. Soc.*, 2024, **146**, 11083–11094.
33 L. E. Nodaraki, A.-M. Ariciu, D. N. Huh, J. Liu, D. O. T. A. Martins, F. Ortu, R. E. P. Winpenny, N. F. Chilton, E. J. L. McInnes, D. P. Mills, W. J. Evans and F. Tuna, Ligand effects on the spin relaxation dynamics and coherent manipulation of organometallic La (II) potential qudits, *J. Am. Chem. Soc.*, 2024, **146**, 15000–15009.
34 J. López-Cabrelles, L. Escalera-Moreno, Z. Hu, H. Prima-García, G. M. Espallargas, A. Gaita-Ariño and E. Coronado, Near isotropic D_{4d} spin qubits as nodes of a Gd(III)-based metal–organic framework, *Inorg. Chem.*, 2021, **60**, 8575–8580.
35 J. Wang, Y. Jing, M. H. Cui, Y. M. Lu, Z. Ouyang, C. Shao, Z. Wang and Y. Song, Spin qubit in a 2D GdIIINaI–based oxamato supramolecular coordination framework, *Chem. – Eur. J.*, 2023, **29**, e202301771.
36 C. Hua, H. M. Tay, Q. He and T. D. Harris, A Series of early lanthanide chloranilate frameworks with a square grid topology, *Aust. J. Chem.*, 2019, **72**, 778–785.
37 C. J. Kingsbury, B. F. Abrahams, J. E. Auckett, H. Chevreau, A. D. Dharma, S. Duyker, Q. He, C. Hua, T. A. Hudson, K. S. Murray, W. Phonsri, V. K. Peterson, R. Robson and K. F. White, Square grid metal–chloranilate networks as robust host systems for guest sorption, *Chem. – Eur. J.*, 2019, **25**, 5222–5234.
38 L. E. Nodaraki, J. Liu, A.-M. Ariciu, F. Ortu, M. S. Oakley, L. Birnoschi, G. K. Gransbury, P. J. Cobb, J. Emerson-King, N. F. Chilton, D. P. Mills, E. J. L. McInnes and F. Tuna, Metal–carbon bonding in early lanthanide substituted cyclopentadienyl complexes probed by pulsed EPR spectroscopy, *Chem. Sci.*, 2024, **15**, 3003–3010.
39 C. A. P. Goodwin, N. F. Chilton, G. F. Vettese, E. M. Pineda, I. F. Crowe, J. W. Ziller, R. E. P. Winpenny, W. J. Evans and D. P. Mills, Physicochemical properties of near-linear lanthanide(II) Bis(silylamide) complexes (Ln = Sm, Eu, Tm, Yb), *Inorg. Chem.*, 2016, **55**, 10057–10067.
40 P. L. Feng, C. C. Beedle, C. Koo, J. Lawrence, S. Hill and D. N. Hendrickson, Origin of magnetization tunneling in single-molecule magnets as determined by single-crystal high-frequency EPR, *Inorg. Chim. Acta*, 2008, **361**, 3465–3480.
41 S. R. Hartmann and E. L. Hahn, Nuclear double resonance in the rotating frame, *Phys. Rev.*, 1962, **128**, 2042–2053.
42 Z. Hu, B.-W. Dong, Z. Liu, J.-J. Liu, J. Su, C. Yu, J. Xiong, D.-E. Shi, Y. Wang, B.-W. Wang, A. Ardavan, Z. Shi, S.-D. Jiang and S. Gao, Endohedral metallofullerene as molecular high spin qubit: diverse rabi cycles in $Gd_2@C_{79}N$, *J. Am. Chem. Soc.*, 2018, **140**, 1123–1130.
43 S. S. Eaton and G. R. Eaton, in *EPR Spectroscopy: Fundamentals and Methods*, ed. D. Goldfarb and S. Stoll, John Wiley & Sons, Chichester, 2018, ch. 9 Relaxation Mechanisms, pp. 175–192.

44 C.-J. Yu, M. D. Krzyaniak, M. S. Fataftah, M. R. Wasielewski and D. E. Freedman, A concentrated array of copper porphyrin candidate qubits, *Chem. Sci.*, 2019, **10**, 1702–1708.

45 A. Jarmola, V. M. Acosta, K. Jensen, S. Chemerisov and D. Budker, Temperature- and magnetic-field-dependent longitudinal spin relaxation in nitrogen-vacancy ensembles in diamond, *Phys. Rev. Lett.*, 2012, **108**, 197601.

46 A. Lunghi, in *Computational Modelling of Molecular Nanomagnets*, ed. G. Rajaraman, Springer, Cham, 2023, ch. 6 Spin–Phonon Relaxation in Magnetic Molecules: Theory, Predictions and Insights, pp. 219–289.

47 H.-J. Lim, S. Welinski, A. Ferrier, P. Goldner and J. J. L. Morton, Coherent spin dynamics of ytterbium ions in yttrium orthosilicate, *Phys. Rev. B*, 2018, **97**, 064409.

48 C. B. Wilson, M. Qi, S. Han and M. S. Sherwin, Gadolinium spin decoherence mechanisms at high magnetic fields, *J. Phys. Chem. Lett.*, 2023, **14**, 10578–10584.

49 K. N. Shrivastava, Theory of spin-lattice relaxation, *Phys. Status Solidi B*, 1983, **117**, 437–458.

50 S. H. Hansen, C. D. Buch, J. B. Petersen, M. Rix, M. U. I. Cervera, A. Strandfelt, R. E. P. Winpenny, E. J. L. McInnes and S. Piligkos, *Chem. Sci.*, 2024, DOI: **10.1039/D4SC05304D**.

51 C. Rajnák and R. Boča, Reciprocating thermal behavior in the family of single ion magnets, *Coord. Chem. Rev.*, 2021, **436**, 213808.

52 V. Tkáč, R. Tarasenko, A. Doroshenko, V. Kavečanský, E. Čižmár, A. Orendáčová, R. Smolko, J. Černák and M. Orendáč, Reciprocating thermal behavior in a magnetic field induced slow spin relaxation of $[Gd_2(H_2O)_6(C_2O_4)_3]\cdot 2.5H_2O$, *Solid State Sci.*, 2023, **136**, 107105.

53 S. Stoll, in *EPR Spectroscopy: Fundamentals and Methods*, ed. D. Goldfarb and S. Stoll, John Wiley & Sons, Chichester, 2018, ch. 11 Pulse EPR, pp. 215–233.

54 E. I. Baibekov, M. R. Gafurov, D. G. Zverev, I. N. Kurkin, A. A. Rodionov, B. Z. Malkin and B. Barbara, Coherent spin dynamics in a gadolinium-doped $CaWO_4$ crystal, *Phys. Rev. B*, 2017, **95**, 064427.

55 S. Takahashi, J. van Tol, C. C. Beedle, D. N. Hendrickson, L.-C. Brunel and M. S. Sherwin, Coherent manipulation and decoherence of S=10 single-molecule magnets, *Phys. Rev. Lett.*, 2009, **102**, 087603.

56 R. M. Brown, Y. Ito, J. H. Warner, A. Ardavan, H. Shinohara, G. A. D. Briggs and J. J. L. Morton, Electron spin coherence in metallofullerenes: Y, Sc, and $La@C_{82}$, *Phys. Rev. B: Condens. Matter Mater. Phys.*, 2010, **82**, 033410.

57 C. E. Jackson, T. Ngendahimana, C.-Y. Lin, G. R. Eaton, S. S. Eaton and J. M. Zadrozny, Impact of counter ion methyl groups on spin relaxation in $[V(C_6H_4O_2)_3]^{2-}$, *J. Phys. Chem. C*, 2022, **126**, 7169–7176.

58 A. Eggeling, J. Soetbeer, L. Fábregas-Ibáñez, D. Klose and G. Jeschke, Quantifying methyl tunneling induced (de) coherence of nitroxides in glassy ortho-terphenyl at low temperatures, *Phys. Chem. Chem. Phys.*, 2023, **25**, 11145–11157.

59 M. J. Amdur, K. R. Mullin, M. J. Waters, D. Puggioni, M. K. Wojnar, M. Gu, L. Sun, P. H. Oyala, J. M. Rondinelli and D. E. Freedman, Chemical control of spin–lattice relaxation to discover a room temperature molecular qubit, *Chem. Sci.*, 2022, **13**, 7034–7045.

60 S. Stoll and A. Schweiger, EasySpin, a comprehensive software package for spectral simulation and analysis in EPR, *J. Magn. Reson.*, 2006, **178**, 42–55.